Check for updates

Fe₃O₄–Pd Janus nanoparticles with amplified dual-mode hyperthermia and enhanced ROS generation for breast cancer treatment†

Xiaowei Ma,‡[abc] Yanyun Wang,‡[a] Xiao-Li Liu,‡[abc] Huijun Ma,[a] Galong Li,[a] Yao Li, [iD][bc] Fei Gao,[a] Mingli Peng, [iD][a] Hai Ming Fan [iD] *[a] and Xing-Jie Liang [iD] *[bc]

Developing multifunctional theranostic nanoplatforms with high tumor therapeutic efficacy is the focus area of nanomedicine. In this study, we have designed Fe₃O₄–Pd Janus nanoparticles (JNPs) with dual-mode magnetic resonance imaging/photoacoustic (MRI/PA) imaging properties for magnetic-photo hyperthermia and chemodynamic therapy simultaneously. Due to the magnetic-photothermal properties of Fe₃O₄ nanoparticles and plasmonic photothermia effect of Pd nanosheets, the combined Fe₃O₄–Pd JNPs can achieve synergistic heating effects of 1 + 1 > 2. It is demonstrated that Fe₃O₄–Pd JNPs reached a higher temperature enhancement under alternating magnetic field (AMF) plus laser irradiation than the corresponding individual modality (only AMF or laser irradiation alone for Fe₃O₄–Pd JNPs) or the sum of two individual modalities. Besides amplified magnetic-photo heating, Fe₃O₄–Pd JNPs also enhanced ROS generation due to the inter-face synergistic effect in producing hydroxyl radicals (•OH), which is realized by Fe₃O₄ nanoparticle-based Fenton reaction and Pd nanosheet-based catalytic properties in the presence of H₂O₂ in an acidic environment. Remarkably, the ROS level could be further elevated under external AMF plus laser irradiation. The *in vivo* anti-tumor effect of Fe₃O₄–Pd JNPs was evaluated on a 4T1 orthotopic mouse breast cancer model. The results showed that Fe₃O₄–Pd JNPs enable complete tumor inhibition without appreciable adverse effects under AMF plus laser irradiation, guided by MRI/PA dual-mode imaging with a high spatial resolution and accuracy. This study provides an alternative way for cancer therapy by on-demand design of high-performance theranostic nanoplatforms according to the characteristics of the tumor microenvironment and the intriguing physiochemical properties of inorganic nanomaterials.

New concepts

Developing effective antitumor agents with high therapeutic outcomes and low side effects in combating cancer remains a formidable challenge. In this work, we report a synergistic magnetic-photo hyperthermia and chemodynamic therapeutic strategy for efficient cancer therapy. We designed biocompatible Fe₃O₄–Pd Janus nanoparticles that are able to achieve significantly high magnetic-photo heating efficiency accompanied by enhanced ROS generation. In addition, Fe₃O₄–Pd Janus nanoparticles also exhibit a dual-modal MRI/PA imaging signal enhancement. *In vivo* antitumor experimentation has demonstrated that the amplified magnetic-photo hyperthermia and chemodynamic therapy by using Fe₃O₄–Pd Janus nanoparticles can exhibit a high tumor-inhibition efficacy towards 4T1 orthotopic breast tumor (inhibition rate 100% at animal model), which was enabled by MRI/PA dual-mode imaging guidance with high spatial resolution and accuracy.

Introduction

Cancer is one of the major causes of mortality worldwide.[1] Curing cancer is as difficult as getting rid of weeds, and scientists have developed a variety of ways to fight cancer. Surgery,[1] radiation therapy,[2,3] and chemotherapy[4–6] are regarded as the main clinical therapy approaches for cancer but suffer from many limitations, such as surgical risks and complications, and serious side effects of radiotherapy and chemotherapy.[7] Moreover, all of these three approaches are accompanied or followed by high local recurrence or distant metastasis, which have rendered cancer cells hard to be completely eradicated and hence poor patient survival rate. Despite years of cancer

[a] *The College of Life Science; Key Laboratory of Synthetic and Natural Functional Molecule Chemistry of the Ministry of Education, College of Chemistry and Materials Science, Northwest University, Xi'an 710069, China. E-mail: fanhm@nwu.edu.cn*

[b] *CAS Key Laboratory for Biomedical Effects of Nanomaterials and Nanosafety, CAS Center for Excellence in Nanoscience, National Center for Nanoscience and Technology of China, No. 11, First North Road, Zhongguancun, Beijing 100190, China. E-mail: liangxj@nanoctr.cn*

[c] *University of Chinese Academy of Sciences, Beijing 100049, China*

† Electronic supplementary information (ESI) available. See DOI: 10.1039/c9nh00233b

‡ Contribution was equal to this work.

treatment, the need for effective cancer treatment remains urgent. Hyperthermia has been pulled in as an adjuvant therapy approach for cancer, and is promising for fighting against cancer.[8,9] Many clinical experiments conducted on breast, cervix, and bladder tumors *etc.* have demonstrated that hyperthermia can intensify the cytotoxic effect of radiation or anti-drugs on tumors.[10,11] However, its non-selective tissue heating could cause potentially severe side effects. Therefore, continuing efforts have been made to develop more effective hyperthermia approach. Nanoparticle-mediated hyperthermia, including nano-photothermal and nano-magnetic therapies, have drawn great attention owing to their good efficacy in tumor ablation and minimal damage to normal tissues.[8] Magnetic hyperthermia therapy (MHT) is a type of medical cancer treatment. Based on Néel and Brownian relaxation of magnetic nanomaterials when exposed to an AMF, heat is produced.[12–15] A variety of MHT clinical trials have been carried out worldwide, and commercial clinical settings have already been released named NanoTherm Therapy (MagForce AG). The most frequently used magnetic nanomaterial is magnetite (Fe_3O_4) nanoparticles because of their favorable biocompatibility. Similarly, in nano-photothermal therapy (PTT), nanomaterials with optical absorption properties could convert light energy into localized heat energy, which are used for tumor or diseased tissue destruction.[16–19] Although they have been applied for years, both MHT and PTT still present some drawbacks. For example, high concentrations of magnetic nanoparticles are required for MHT,[20] which remains a strong uncertainty in clinical settings. The limited tissue penetration of light is the main problem in PTT. Hence, to combine MHT with PTT into an integrated nanocomposition is a popular dual-mode curative treatment approach to overcome the main shortcomings found in individual treatment types, as well as to realize high-efficiency synergistic therapeutic performance.

Various types of multifunctional theranostic nanoplatforms have been developed for combination heating therapy. For example, Yan *et al.* developed a multifunctional theranostic nanoplatform, which was composed of Fe_3O_4 nanoparticles, Cyanine7 (Cy7), poly(3,4-ethylenedioxythiophene):poly(4-styrene-sulfonate) (PES), and 2-deoxyglucose (2-DG)-polyethylene glycol to realize photo-magnetic hyperthermia *in vivo*.[20] Yang *et al.* utilized Fe_3O_4 nanoparticles and PbS/CdS quantum dots to achieve synergistic dual-mode hyperthermia therapy for cancer.[21] Most of the studies focused on the construction of nanomaterials with high MHT-PTT heating efficiency for killing cancer cells, or of particular interest in developing multifunctional theranostic nanoplatforms which combine an appropriate diagnostic modality with a dual-mode (magnetothermal and photothermal) heating treatment together to achieve "precision medicine". Although a multi-mode imaging-guided MHT-PTT heating modality for cancer therapy can be achieved by Fe_3O_4-based multifunctional nanocomposites, the concomitant biological effects of this multi-composite nanoplatform for killing cancer cells is still worthy of deep investigation. For instance, as commonly used MHT agents, Fe_3O_4 nanoparticles are also classical Fenton nanoagents, based on their specific catalytic

capability triggered in the tumor microenvironment by generating reactive oxygen species (ROS), *e.g.*, toxic hydroxyl radicals ($^\bullet OH$).[22] Up-regulation of $^\bullet OH$ in cancer cells can lead to the damage of DNA and lipid peroxidation, and induce tumor cell apoptosis. However, besides heating effects, the biological effects of Fe_3O_4-based multifunctional nanocomposites generated after being exposed to an external source of energy (*e.g.*, laser or AMF or both) have not been fully investigated. It is a neglected area that dual-mode (magnetothermal and photothermal) heating treatment associated ROS generation could be applied to achieve multifunctional nanotheranostic platforms.

Very recently, it has been found that inorganic Janus nanoparticles that integrate the components with distinct physical or chemical properties could provide exciting characteristics for advanced cancer theranostics.[23] Magnetic iron oxide nanoparticles (MIONs) are significant biomedical inorganic nanoparticles already in use as magnetic resonance imaging (MRI) and magnetic hyperthermia agents in pre-clinical and clinical settings.[24–26] Meanwhile, the Fenton reactions between iron (II or III) derived from MIONs and H_2O_2 that produce and accumulate ROS have been widely accepted.[22] The metal palladium (Pd) possesses extraordinary mechanical, catalytic, and electronic properties, and is mainly used in industrial processes. Unlike the other commonly used noble metal nanoparticles such as gold and silver, Pd nanomaterials possess excellent stability.[27,28] However, investigations on Pd nanomaterials in cancer theranostic applications are rare, which results from the fact that the majority of chemically-fabricated Pd nanomaterials display localized surface plasmon resonance (SPR) in the UV and visible spectral regions. This is out of the photoacoustic imaging and photothermal therapy favorable near infrared (NIR) region.[27,29] Recently, a great discovery has been made by Zheng *et al.* that a strong and tunable SPR band in the NIR spectral region was observed for hexagonal Pd nanosheets (Pd NSs), which opens a door for applying Pd NSs with SPR in the NIR region in biomedicine. More importantly, Wen *et al.* observed that Pd nanomaterials could produce $^\bullet OH$ in acidic conditions.[28] Considering the unique physical property of MIONs and Pd NSs, integration of MIONs and Pd NSs into one entity is expected to be a new high-efficiency magnetic-photo heating agent and will generate reactive oxygen species (ROS), which will not only integrate their merits and overcome intrinsic shortcomings, but also increase the functionalities that facilitate their usage in nanotheranostics.

In the present study, we established Fe_3O_4–Pd Janus nanoparticles (JNPs) by combination of both MIONs and Pd NSs for synergistic dual-modal imaging and hyperthermia treatment, according to their outstanding magnetic properties and NIR surface plasmon resonance properties. Motivated by their excellent magnetic-photo performance in an aqueous solution, and good biocompatibility in cells, we delivered Fe_3O_4–Pd JNPs by intravenous administration to an orthotopic 4T1 breast tumor for amplified dual-mode magnetic-photo hyperthermia treatment under the proper guidance of dual-modality imaging (shown in Scheme 1). The enhanced ROS generation for Fe_3O_4–Pd

Scheme 1 A schematic illustration of the design and application of Fe$_3$O$_4$–Pd JNPs for MRI/PA dual-modal imaging guided amplified dual-mode hyperthermia and enhanced ROS mediated antineoplastic therapy of orthotopic 4T1 breast cancer.

JNPs after AMF plus NIR laser irradiation exposure *in vitro*, and amplified therapeutic effects for magnetic-photo heating *in vivo* were observed. The tumor was completely eliminated on day 18, monitored under MRI/PA dual-mode imaging with a high spatial resolution and accuracy. This study elaborated the significant enhancement of ROS generation and amplified dual-mode hyperthermia for Fe$_3$O$_4$–Pd JNPs in the fight against cancer, which provides a useful way of designing multifunctional theranostic nanoplatforms with desired properties in biomedical applications.

Experimental

Materials

FeO(OH) was from Aldrich (iron(III) oxide hydroxide; 99.5%), oleic acid (90%), 1-octadecene (99.9%), dopamine, tetrahydrofuran (THF), hydrochloric acid (HCl, 37%), palladium(II) acetylacetonate (Pd(acac)$_2$, 99%), polyvinyl pyrrolidone (PVP), *N,N*-dimethylacetamide, 1-ethyl-3-(3-dimethylaminopropyl)carbodiimide hydrochloride (EDC, 90%), *N*-hydroxysuccinimide (NHS, 90%), HOOC-PEG-COOH (molecular weight 5000), 2′,7′-dichlorodihydrofluorescein diacetate (DCFH-DA), methanol (99.9%), deionized water (DI water), H$_2$O$_2$ (30%), sodium acetate buffer solution, methylene blue (MB, 82%), cell counting kit-8 (CCK-8), RPMI-1640 medium, fetal bovine serum (FBS), and penicillin/streptomycin were purchased from Sigma-Aldrich, and NaBr was purchased from Shanghai deber biotechnology limited company.

Synthesis of Fe$_3$O$_4$–Pd JNPs

Pd NSs and Fe$_3$O$_4$ NPs were firstly prepared separately. The Pd NSs were prepared as previously reported.[29] Hydrophobic Fe$_3$O$_4$ NPs were firstly prepared and then were surface modified by dopamine to obtain Fe$_3$O$_4$ NP aqueous solutions. Hydrophobic Fe$_3$O$_4$ NPs were prepared as reported by the thermal decomposition of iron carboxylate salts method.[30] Hydrophilic Fe$_3$O$_4$ aqueous solutions were prepared by using dopamine to displace oleic acid on the surface of the as-synthesized hydrophobic Fe$_3$O$_4$ NPs. In brief, 50 mg dopamine was dissolved in a mixture of DI water (0.3 mL) and THF (4.7 mL). The mixture was heated to 50 °C under Ar flow. Then, 2 mL Fe$_3$O$_4$ NPs solution (in THF) was added and co-incubated for another 5 h at 50 °C. After the reaction was complete, HCl (1 M) was added and the precipitate was collected by centrifugation (8000 rpm, 10 min). The sample was re-dispersed in DI water.

Fe$_3$O$_4$–Pd JNPs were obtained by mixing Pd NSs and Fe$_3$O$_4$ NP aqueous solutions (Fe$_3$O$_4$/Pd molar ratio is 1:1) under magnetic stirring. After 1 h, EDC (12 mg mL^{-1}) and NHS (10 mg mL^{-1}) were added to activate the amino group, and then mixed with 1 mL HOOC-PEG-COOH aqueous solution. The reaction was left in the shaker overnight at room temperature. The obtained products were purified by dialyzing against Millipore water for three days in a dialysis sac (molecular weight cut-off = 10 kDa). The number of HOOC-PEG$_{5000}$-COOH on each Fe$_3$O$_4$–Pd JNP is approximately 800.

Characterizations

The samples' size and shape were characterized using transmission electron microscopy (TEM, FEI Talos 200s). The crystal

phase of the samples was examined by powder X-ray diffracto-metry (Bruker D8 Advanced Diffractometer System) with Cu Ka radiation. UV-vis-NIR spectra were obtained using a T6 UV-vis-NIR spectrophotometer. The magnetic properties were characterized by a LakeShore Model 7407 vibrating sample magnetometer (VSM). Dynamic light scattering (DLS) and zeta potential was measured using a particle size analyzer (Zetasizer Nano ZS-90, Malvern). The concentrations of Fe and Pd were quantified using an inductively coupled plasma mass spectro-metry (ICP-MS, NexION 300×). Heating curves were recorded by an IR thermal camera (FLIR T200).

Cytotoxicity assay

4T1 breast cancer cells were cultured in RPMI-1640 medium containing 10% FBS and 1% penicillin/streptomycin. 4T1 cells (2×10^4 cells per well) were seeded on 96-well plates, cultured at 37 $^\circ$C in a 5% CO_2 atmosphere. And then, 4T1 cells were incubated with Fe_3O_4–Pd JNPs at various concentrations (0, 12.5, 25, 50, 100, 200 $\mu g\ mL^{-1}$) for 24 h. After 24 h, the wells were added with CCK-8 and further incubated for another 4 h. The absorbance readings were conducted at 450 nm using a FluoStar Optima microplate reader.

In vitro magnetic-photo heating

Fe_3O_4–Pd JNPs were treated with AMF plus 808 nm laser (0.5 W cm^{-2}, 8 min), treated with AMF alone or 808 nm laser alone was as control. 1 mL Fe_3O_4–Pd JNPs at different concentrations (0, 50, 100, 200 $\mu g\ mL^{-1}$) were separately placed inside the Cu coil in 15 mL tubes. Both the optical fiber connected to a multimeter and the infrared (IR) thermal imaging camera measured and recorded the temperature increase in real time.

Detection of hydroxyl radicals

CH_3COONa buffer solution containing 50 $\mu g\ mL^{-1}$ MB, 8 mM H_2O_2, and 1 mg mL^{-1} materials was allowed to stand at 37 $^\circ$C. The •OH-induced MB degradation was monitored by the absorbance change at 664 nm at different time points and various pH values.

Intracellular ROS formation

4T1 cells were placed at a density of 6×10^4 cells per well into 24-well plates and were incubated for 24 h. Then, cells were treated by Fe_3O_4–Pd JNPs for 12 h. The cells were washed with PBS three times and treated with AMF plus 808 nm laser (0.5 W cm^{-2}, 2 min). The treated cells were incubated with 2′,7′-dichlorodihydrofluorescein diacetate (DCFH-DA, 10 μM) for 30 min. The cells were washed with PBS three times again, and the fluorescence intensity was recorded by Zeiss LSM 710 (excitation: 488 nm, emission: 525 nm).

Animals and tumor model

All of the animal experiments were conducted according to the guidelines that were approved by the Institutional Animal Care and Use Committee (Permit No: 2011-0039) at Peking University, Beijing, China. Female BALB/c mice (6–8 weeks old, 16–18 g) were obtained from Weitong Lihua Experimental Animal Technology Co. Ltd, Beijing, China. 4T1 tumor cells (5×10^6) were injected

into the breast fat pad below the abdomen of each mouse. The mice were anesthetized with isoflurane (1.5%) throughout the experiment.

In vitro MRI/PA tests

T_2-weighted MR imaging of Fe_3O_4–Pd JNPs fully filled in the tube, with different Fe_3O_4 concentrations (0, 0.06, 0.13, 0.25, 0.5, 1 mmol L^{-1}), was performed using a 7T MR imaging instrument (BioSpec 70/20 USR, Bruker, Germany). T_2 relaxation times were measured by a multi-echo spin-echo sequence. The relaxation rates r_2 ($r_2 = 1/T_2$) were calculated according to the measured T_2 values.

For the PA imaging of Fe_3O_4–Pd JNPs in vitro, 0.5 mL of Fe_3O_4–Pd JNPs solution with various Pd concentrations (0, 1, 2, 3, 4 $\mu g\ mL^{-1}$) was added into the agarose phantom container, and installed in the multispectral optoacoustic tomography system (MSOT, model in Vision 128, iThera Medical GmbH, Munich, Germany) for signal acquisition. The PA imaging signals of Fe_3O_4–Pd JNPs were collected under an irradiation range from 680 to 900 nm.

In vivo MRI/PA dual-mode imaging

For MR and PA imaging in vivo, BALB/c mice were injected with Fe_3O_4–Pd JNPs (200 μL of 0.6 mg mL^{-1} [Fe] for each mouse) by the tail vein. MR and PA signals were collected at different time points (pre-, 2, 4, 8, 12 and 24 h). In vivo MRI was performed on a 7.0 T small animal MRI instrument (BioSpec 70/20 USR, Bruker, Germany). MRI images were acquired using T_2-Turbo RARE sequence with parameters as follows: TR = 2900 ms, TE = 40.06 ms, field of view = 35 mm $\times$ 35 mm, matrix size = 256 $\times$ 256, flip angle = 90° and NEX = 3. In vivo PA images were acquired on a multispectral optoacoutic tomography system (MSOT inVision 128, iThera medical, Germany). The mice were anesthetized, and placed into a water bath (maintain body temperature at 37 $^\circ$C) for tumor imaging.

Magnetic-photo hyperthermia therapy

When the tumor volume reached 60 mm^3, the mice were randomly divided into six groups (n = 5 per group): (1) normal saline, (2) Fe_3O_4–Pd JNPs (6 mg kg^{-1}), (3) AMF (300 kHz; 300 Oe) + laser (808 nm, 0.5 W cm^{-2}), (4) Fe_3O_4–Pd JNPs with MHT, (5) Fe_3O_4–Pd JNPs with PTT, and (6) Fe_3O_4–Pd JNPs with MHT-PTT. The tumors were treated once with injection of samples and once with external energy exposure (8 min). During the treatment period, thermal images of the mice were recorded by an IR thermal imaging camera. The tumor sizes were measured after treatments by a digital caliper every 2 days for 18 days. The tumor volume was calculated according to the following formula: width^2 $\times$ length/2. Body weights were monitored every 2 days for 18 days. At the end, the tumors were resected, weighed and photographed. Percent survival of the mice bearing tumors after treatment was monitored.

Histological analysis

After the in vivo hyperthermia studies, major organs, including the lungs, spleen, heart, and liver, were excised and preserved

in 10% formalin for histological sectioning. H&E staining was performed to examine using an optical microscope.

Statistical analysis

The Graph Pad Prism Version 5.0 (GraphPad Software) was used for data analysis. The one-way ANOVA with Tukey's post-hoc test was used for analysis of different groups. Data are reported as mean values $\pm$ SEM. *indicates P-values of < 0.05, and **indicates P-values of < 0.01. Both were considered statistically significant.

Results and discussion

MIONs have been demonstrated to act as powerful negative contrast agents and magnetic hyperthermia agents because of their superior magnetic properties. Due to their optimal size for high T_2 shortening effects and MHT efficacy, mono-dispersed 15 nm Fe_3O_4 NPs (at the superparamagnetism/ferromagnetism transition stage) were chosen in this work as T_2-weighted MRI contrast agents and magnetic hyperthermia agents.[15,31–33] Ultrathin two-dimensional (2D) Pd NSs have appeared as a significant class of nanomaterial with enormous potential particularly in cancer theranostics. Compared with larger-sized Pd NSs, it is reported that smaller-sized Pd NSs with an edge length of 13 nm exhibited more advanced PA imaging and PTT effects upon ultralow laser irradiation.[27,29] Due to the excellent magnetic properties of Fe_3O_4 NPs and high NIR absorption ability of Pd NSs, the resultant Fe_3O_4–Pd JNPs could be used as multifunctional nanoprobes for MRI/PA dual-mode imaging as well as magnetic-photo thermotherapy *in vivo* with high resolution, accuracy and efficiency. High quality mono-dispersed Fe_3O_4 NPs and Pd NSs were firstly synthesized as previously reported, and Fe_3O_4–Pd JNPs were then fabricated by electrostatic adsorption between Fe_3O_4 NPs and Pd NSs. As shown in Fig. 1a, the synthesized Fe_3O_4–Pd JNPs had uniform size and morphology, in which one component was spherical Fe_3O_4 NPs with an average diameter of 15 nm (Fig. S1a, ESI†), and the other was hexagonal Pd NSs with an edge length of 13 nm and 1.8 nm thickness on average (Fig. S1b, ESI†). The size of Fe_3O_4–Pd JNPs is considerably uniform with a narrow distribution (SD $< 1.533\%$). The XRD pattern (Fig. S1c and d, ESI†) indicated that both Fe_3O_4 NPs and Pd NSs are crystalline and matched well with the standard Fe_3O_4 diffraction data (JCPDS card no. 19-0629) and Pd diffraction data (JCPDS card no. 05-0681), respectively. The high-resolution TEM (HRTEM) image (Fig. 1b and c) showed that the lattice spacing of Fe_3O_4 in the Fe_3O_4–Pd JNPs was 0.21 nm, which is in agreement with the (400) lattice plane of Fe_3O_4. Moreover, a lattice fringe of 0.226 nm corresponding to the (100) plane of Pd further confirmed the uniform structure and good single crystallization of Fe_3O_4–Pd JNPs.

To prevent aggregation of Fe_3O_4–Pd JNPs in physiological conditions and minimize cytotoxicity, $HOOC$-PEG_{5k}-$COOH$ (abbreviated as PEG) was grafted on the surface of Fe_3O_4–Pd JNPs. The hydrodynamic size of Fe_3O_4–Pd JNPs after grafting
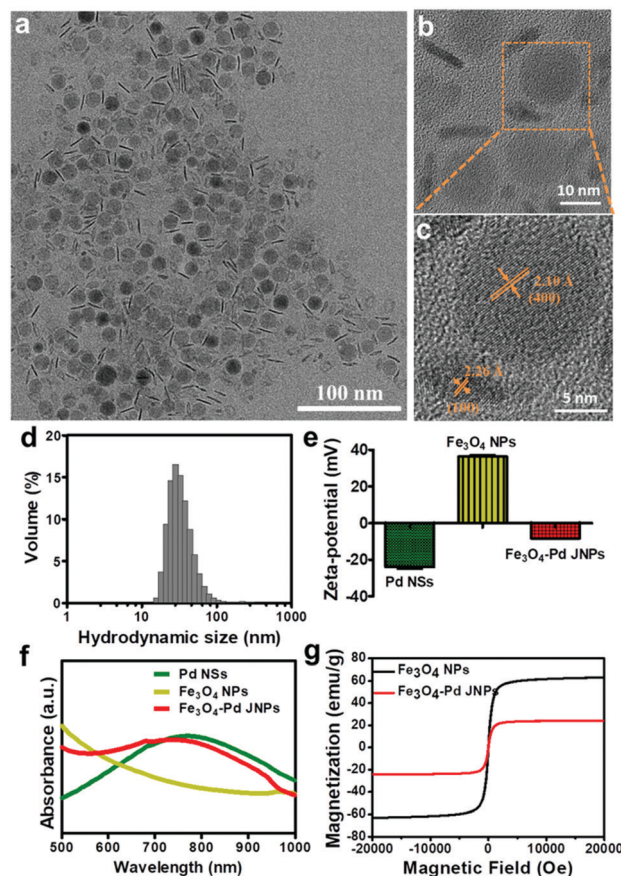

Fig. 1 (a) TEM image, (b) enlarged TEM image and (c) HRTEM image of Fe_3O_4–Pd JNPs. (d) Hydrodynamic size of Fe_3O_4–Pd JNPs. (e) Zeta potential of Pd NSs, Fe_3O_4 NPs and Fe_3O_4–Pd JNPs. (f) UV-vis-NIR absorption spectra of Pd NSs, Fe_3O_4 NPs and Fe_3O_4–Pd JNPs. (g) Magnetization hysteresis loops of Fe_3O_4–Pd JNPs.

PEG was around 35 nm with narrow size distribution (Fig. 1d). As is shown in Fig. 1e, the zeta potential of Fe_3O_4–Pd JNPs was -8.43 mV, which further demonstrated that PEG was modified onto the surface of Fe_3O_4–Pd JNPs. It also confirmed the successful combination of positively charged Fe_3O_4 NPs ($+38.2$ mV) with amino groups and negatively charged Pd NSs (-25 mV) with carboxyl groups. After PEG modification, the Fe_3O_4–Pd JNPs exhibited significantly improved stability in different physiological solutions such as DI water, $1 \times$ PBS, RPMI-1640 medium containing 10% FBS, as well as normal saline, and was very stable for at least 12 days at 37 °C (Fig. S2, ESI†).

To further confirm the formation of Fe_3O_4–Pd JNPs, we measured the UV-vis absorbance of Pd NSs, Fe_3O_4 NPs, and Fe_3O_4–Pd JNPs. As is shown in Fig. 1f, Pd NSs in water displayed a characteristic absorption peak at 765 nm and the characteristic band of Pd is at 725 nm for Fe_3O_4–Pd JNPs, which was slightly blue-shifted, indicating the interactions between Fe_3O_4 NPs and Pd NSs by electrostatic interaction. The maximum absorptions of Fe_3O_4–Pd JNPs implied that the optimal 808 nm NIR excitation source can be used to irradiate Fe_3O_4–Pd JNPs for PTT.

The magnetic properties of Fe_3O_4–Pd JNPs were evaluated using a VSM. M–H curves of Fe_3O_4–Pd JNPs taken at room temperature are shown in Fig. 1g. It clearly showed that Fe_3O_4–Pd JNPs exhibited superparamagnetic properties with no coercivity at room temperature. The magnetization is 24.4 emu g^{-1} at 20 kOe. The reduced magnetization compared with pure Fe_3O_4 NPs ($\sim$60 emu g^{-1}) resulted from the decreased effective weight fraction of the magnetic components.

Motivated by the excellent magnetic-photo properties of Fe_3O_4–Pd JNPs, the heating effects of Fe_3O_4–Pd JNPs were then evaluated by using a magnetic-photo induction heating system (Fig. 2a). Samples were fixed into a Cu coil; and exposed to AMF plus 808 nm NIR laser irradiation. The temperature change of the solution was recorded by an optical fiber connected to a multimeter and an IR thermal imaging camera. In order to integrate magnetic-photo hyperthermia, three heating modes were compared: (i) MHT, AMF (amplitude, 300 Oe; frequency, 350 kHz) for 8 min; (ii) PTT, 808 nm NIR laser (0.5 W cm^{-2}) for 8 min; and (iii) MHT-PTT dual-mode, both AMF and 808 nm NIR laser, for 8 min. Under AMF exposure, the aqueous suspension of Fe_3O_4–Pd JNPs showed little magnetic hyperthermia effect and the temperature change of Fe_3O_4–Pd JNPs under AMF within 480 s was 5 °C (Fig. 2b). Under 808 nm NIR laser

irradiation (0.5 W cm^{-2}), the Fe_3O_4–Pd JNPs showed excellent heating effects with apparent concentration-dependent temperature increase (Fig. 2c). The temperature change of Fe_3O_4–Pd JNPs under 808 nm NIR within 480 s was 20 °C at the concentration of 200 μg mL^{-1} [Fe + Pd]. For MHT and PTT dual-mode, the temperature increased to 29.1 °C, 33.4 °C and 32.6 °C with 50 μg mL^{-1}, 100 μg mL^{-1} and 200 μg mL^{-1} [Fe + Pd] within 480 s, respectively (Fig. 2d). It was obvious that the temperature change for dual-mode hyperthermia was higher than the two individual modalities, and even higher than the sum of the two individual modalities. In addition, it has been reported that Fe_3O_4 NPs have both magnetic thermal and photothermal effects, the temperature change of Fe_3O_4 NPs under AMF plus 808 nm NIR within 480 s was 11 °C at the same Fe concentration (100 μg mL^{-1} [Fe]) (Fig. S3, ESI†), which is 66% lower than that of Fe_3O_4–Pd JNPs (32.6 °C). Fig. 2e showed the corresponding thermal images of Fe_3O_4–Pd JNP solutions of different concentrations under AMF plus NIR laser irradiation. It could be seen that the solution temperature increased with the increase of Fe_3O_4–Pd JNP concentration. The temperature increase of Fe_3O_4–Pd JNPs with different concentrations after 480 s of each heating strategy (AMF, laser, and dual-mode) was studied and is presented in Fig. 2f. Remarkably, the temperature increase of Fe_3O_4–Pd JNPs under dual-mode heating exceeded either PTT or MTT heating alone, which confirmed the synergistic effect of the dual-mode heating strategy, while PTT was the major contribution of heating in the dual-mode heating.

MIONs have been considered as negative (T_2) contrast agents and magnetic hyperthermia agents. To assess the T_2 MR imaging performance of Fe_3O_4–Pd JNPs, T_2-weighted MR images of Fe_3O_4–Pd JNPs (with different Fe concentrations) were acquired by a 7T MR scanner. Fe_3O_4 NPs with the same Fe concentration as Fe_3O_4–Pd JNPs were used as a control. Both Fe_3O_4–Pd JNPs and Fe_3O_4 NPs presented dose-dependent darkening effect as a negative T_2 MR contrast agent. While free Fe_3O_4 NPs possessed more obvious reduction in T_2 relaxation time compared with Fe_3O_4–Pd JNPs, which was clearly displayed by the much darker images at the designated Fe concentration from 0.06 to 1 mM (Fig. 3b). The transverse relaxivity (r_2) calculated was 141.38 mM^{-1} s^{-1} for Fe_3O_4–Pd JNPs, which was lower than that of Fe_3O_4 NPs (216 mM^{-1} s^{-1}) (Fig. 3a). The reason for the decreased relaxivity of Fe_3O_4–Pd JNPs may be the decreased saturation magnetization (M_s). Besides being used as MRI contrast agents, Fe_3O_4–Pd JNPs can also be used for PA imaging due to the prominent absorbance band in the NIR region of Pd NSs, which encouraged us to exploit their PA imaging properties. The PA signal of Fe_3O_4–Pd JNPs was recorded by a multispectral optoacoustic tomography (MSOT) imaging system (Fig. 3d). The PA signal intensities increased linearly with Pd concentrations for both Fe_3O_4–Pd JNPs and pure Pd NSs, which suggested that Fe_3O_4–Pd JNPs could serve as efficient contrast agents. The slope of PA intensity vs. Pd concentration of Fe_3O_4–Pd JNPs was 182.9, which was higher than that of pure Pd NSs (121.7) (Fig. 3c). All of the in vitro results suggested that Fe_3O_4–Pd JNPs could be used as MRI and PA imaging contrast agents.

Fig. 2 Magnetic-photo dual-mode hyperthermia in aqueous solution. (a) Schematic diagram of the magnetic-photo dual-mode hyperthermia measurement system. Time dependent heating profiles of Fe_3O_4–Pd JNPs at various concentrations (b) under AMF (300 Oe; 350 kHz), (c) under 808 nm laser irradiation at a power density of 0.5 W cm^{-2}, and (d) under AMF plus 808 nm laser. (e) Thermal images acquired by the IR camera of Fe_3O_4–Pd JNPs at different concentrations under AMF plus 808 nm laser. (f) Average temperature increase recorded for Fe_3O_4–Pd JNPs under the three heating protocols.

Fig. 3 (a) T_2 relaxation rate ($1/T_2$) as a function of Fe concentration for Fe$_3$O$_4$–Pd JNPs and pure Fe$_3$O$_4$ NPs, respectively. (b) T_2-weighted MR images of Fe$_3$O$_4$–Pd JNPs and pure Fe$_3$O$_4$ NPs in aqueous solution at different Fe concentrations. (c) Linear relationship between PA signal intensity with Fe$_3$O$_4$–Pd JNPs and pure Pd NSs, respectively. (d) PA imaging phantoms of Fe$_3$O$_4$–Pd JNPs and pure Pd NSs embedded in agar gel cylinders at various Pd concentrations. (e) T_2-weighted MR images *in vivo* of 4T1 tumor-bearing mice at various time points before and after intravenous injection of Fe$_3$O$_4$–Pd JNPs. (f) T_2 value at the tumor site at different time points post-injection. (g) PA images *in vivo* of 4T1 tumor-bearing mice taken at different times after intravenous injection of Fe$_3$O$_4$–Pd JNPs. (h) Average PA intensity arising from the tumor area before and after intravenous injection of Fe$_3$O$_4$–Pd JNPs.

Attributed to the excellent T_2-weighted MRI and PA dual contrast-enhancing performance of Fe$_3$O$_4$–Pd JNPs, the *in vivo* tumor accumulation behavior of Fe$_3$O$_4$–Pd JNPs was explored. Before *in vivo* experiments, a cell viability assay was conducted and revealed that Fe$_3$O$_4$–Pd JNPs had minimal cytotoxic effects. It was safe to use as high as 100 μg/Fe mL of Fe$_3$O$_4$–Pd JNPs on cells (Fig. S4, ESI†). 200 μL of Fe$_3$O$_4$–Pd JNPs (equivalent to a dose of 3.0 mg kg^{-1} Fe or Pd/mouse body) in normal saline was injected intravenously into orthotopic 4T1 tumor-bearing mice, followed by MRI imaging at various post-injection time points. As presented in Fig. 3e, the evidently darkened T_2 signals indicated enhanced MRI effectiveness in the tumor over time. At 4 h post-injection, the tumors became more distinguishable

from the other organs. Quantitative MRI data of the tumors at 4 h post-injection showed 14% and 7% T_2 signal decays compared to 2 h and 6 h post-injection, respectively (Fig. 3f), suggesting that 4 h post-injection is the time point with the highest signal. For a more thorough investigation on the trafficking profile of Fe$_3$O$_4$–Pd JNPs, PA images based on the intrinsic PA signal of Pd NSs were also studied. The signal intensity in the tumor gradually increased with time because of the accumulation of Fe$_3$O$_4$–Pd JNPs *via* the EPR effect (Fig. 3g). Quantification analysis verified the remarkable increase in PA signal over time at the tumor site, which was in accordance with the MRI results (Fig. 3h).

Fe$_3$O$_4$–Pd JNPs have high catalytic activity of the decoloration of methylene blue (MB) through the decomposition of H$_2$O$_2$ to •OH in Fenton-like reactions, and Pd nanostructures can also induce •OH production in the presence of H$_2$O$_2$. The ROS generation capabilities of Fe$_3$O$_4$ NPs, Pd NS, and Fe$_3$O$_4$–Pd JNPs at different pH values were evaluated by monitoring the time-dependent degradation of MB (Fig. 4a and Fig. S5, ESI†). The absorbance intensity of MB showed a time-dependent decrease in the presence of Fe$_3$O$_4$ NPs, Pd NS, and Fe$_3$O$_4$–Pd JNPs at pH 5.0. The 664 nm absorbance peak of MB exhibited a 62.9% and 84.4% decrease after 24 h for Pd NSs and Fe$_3$O$_4$–Pd JNPs, respectively. Little change was observed for Fe$_3$O$_4$ NPs. The slightly higher ROS production ability of Fe$_3$O$_4$–Pd JNPs than that of either Pd NSs or Fe$_3$O$_4$ NPs may be due to the dual-modal ROS generation capability of Pd NSs and Fe$_3$O$_4$ NPs. Furthermore, The ROS generation capability of Fe$_3$O$_4$–Pd JNPs when exposed to AMF or 808 nm laser or both was also estimated. As shown in Fig. 4b, in the presence of Fe$_3$O$_4$–Pd JNPs, the MB absorption at 664 nm significantly decreased under external energy exposure, suggesting the efficient generation of ROS with external energy exposure. When AMF plus laser irradiation was applied, 99.5% decrease in intensity was observed. In addition, we also evaluated the ROS generation capability of Fe$_3$O$_4$ NPs, Pd NS, and Fe$_3$O$_4$–Pd JNPs at pH 6.5 and 7.4, respectively. When the pH was at 6.5, the absorbance intensity of MB at 664 nm showed an intense decrease. As shown in Fig. S5a and b (ESI†), only a 40.1% decrease of the MB absorbance peak, and a 64.5% decrease with AMF and laser exposure was observed. Further increasing the pH to 7.4, no difference in the absorbance intensities of MB was observed (Fig. S5c and d, ESI†). These results suggested that Fe$_3$O$_4$–Pd JNPs could activate H$_2$O$_2$ decomposition by producing a great many •OH. And the acidic condition was required for effective Fenton reaction. Such an obvious enhancement resulted from the synergistic effect of Fe$_3$O$_4$ and Pd components at the interface, which was believed to stabilize the excess •OH. More importantly, the external energy could promote the enhancement of ROS generation, and showed a higher and sustaining •OH generation rate.

The capacity of Fe$_3$O$_4$–Pd JNPs in elevating the intracellular ROS level was investigated by using a fluorescent ROS probe (dichlorofluorescein-diacetate, DCFH-DA). In the presence of ROS, DCFH is oxidized to DCF to emit bright green fluorescence. The cells were treated with PBS or Fe$_3$O$_4$–Pd JNPs under
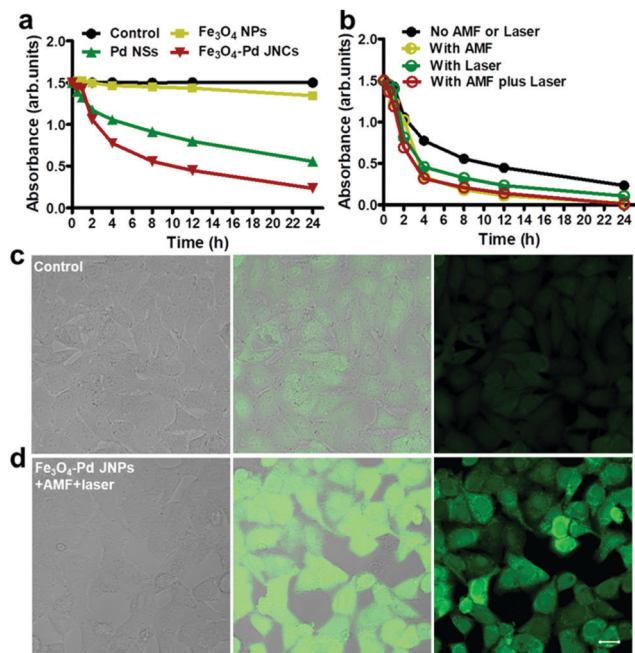
Fig. 4 (a) Decay curves of MB absorption at 664 nm in different solutions as a function of time. (b) Decay curves of MB absorption at 664 nm for Fe_3O_4–Pd JNPs under AMF or laser or both for 8 min, as a function of time. (c and d) CLSM images of 4T1 cells incubated with complete media (control) of Fe_3O_4–Pd JNPs containing media under AMF plus laser treatment. Generation of ROS was monitored using DCFH-DA (green). Scale bars for all images are 20 μm.

Fig. 5 (a) Thermal IR imaging of 4T1 tumor-bearing mice after intravenous injection of Fe_3O_4–Pd JNPs exposed to AMF, 808 nm laser or AMF plus 808 nm laser ($N = 5$). (b) Growth curves of tumor volume of mice from different groups. (c) Tumor mass of different groups. (d) Digital photos of tumor tissues harvested from mice at the end of treatment. (e) Body weight curves of mice from different groups. One-way ANOVA with Tukey's multiple comparisons test was used to analyse differences among groups. Data are reported as mean values ± SEM. *indicates P-values of <0.05, and **indicates P-values of <0.01. Both were considered statistically significant.

AMF plus 808 nm laser irradiation. It was obvious that cells treated with Fe_3O_4–Pd JNPs under AMF plus 808 nm laser irradiation exhibited significant green fluorescence (Fig. 4d), indicating that Fe_3O_4–Pd JNPs could be efficiently internalized into the cells and then generate ROS. For the control group, all of the cells showed negligible fluorescence (Fig. 4c).

Encouraged by the amplified dual-mode hyperthermia and enhanced ROS generation effects of Fe_3O_4–Pd JNPs, we employed Fe_3O_4–Pd JNPs for MHT-PTT combinatorial therapy *in vitro* and *in vivo*. To prove the therapy effects of Fe_3O_4–Pd JNPs *in vitro*, the 4T1 cells were stained with calcein-AM/PI after receiving different treatments. Live and necrotic cells appeared green and red, respectively. As shown in Fig. S6, ESI,† most of the 4T1 cells treated by MHT + PTT were necrotic cells, evidenced by the appearance of strong red fluorescence. For the MHT or PTT group, there was still the appearance of green fluorescence, indicating that the MHT or PTT alone exhibited relatively weak killing effects on 4T1 cells.

Before performing the *in vivo* animal antitumor experiments, the biodistribution of Fe_3O_4–Pd JNPs in 4T1 tumor-bearing Balb/c mice was studied. The results showed that Fe_3O_4–Pd JNPs exhibited low distribution in the heart, liver, brain, and kidneys, and relatively high distribution in the spleen. The tumor uptake was 249 μg Fe per g tumor at 24 h after intravenous administration (Fig. S7, ESI†). *In vivo* experiments were carried out on six groups of orthotopic 4T1 breast tumor bearing mice, the treatment plans were as follow: (1) normal saline (control),
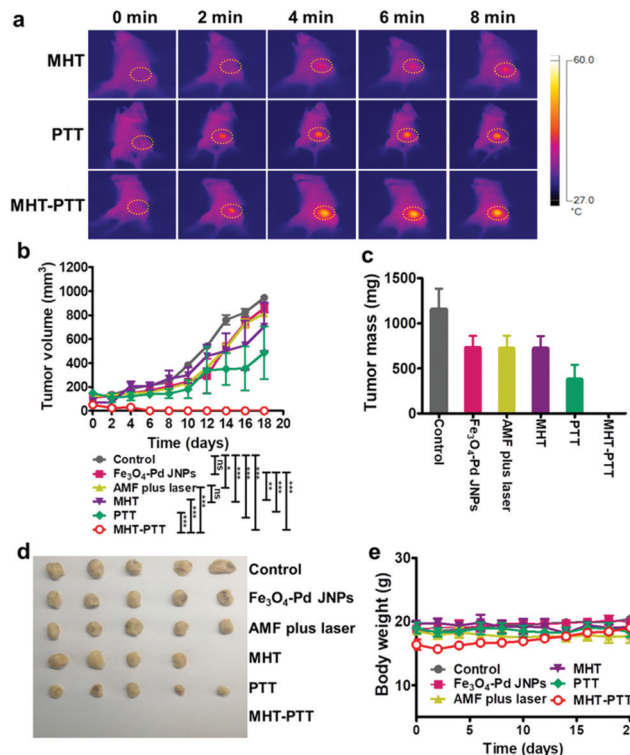
(2) Fe_3O_4–Pd JNPs, (3) AMF + 808 nm laser irradiation, (4) Fe_3O_4–Pd JNPs + AMF (MHT), (5) Fe_3O_4–Pd JNPs + 808 nm laser irradiation (PTT), and (6) Fe_3O_4–Pd JNPs + AMF + 808 nm laser irradiation (MHT + PTT). 4 hours after injection, when maximum samples accumulated in tumors from the quantitative results of MRI and PA, AMF exposure or laser radiation was applied at the tumor site, and the tumor surface temperature was monitored using an IR thermal camera (Fig. 5a). The tumor temperature reached 42 °C (6.4 °C increase) for MHT and 48.5 °C (12.5 °C increase) for PTT. While the tumors from the MHT + PTT group showed a significant temperature increment up to 52.4 °C (26.2 °C increase), which further suggested a synergistic effect generated by the Fe_3O_4–Pd JNPs. We further evaluated the anti-tumor efficacy of each treatment by monitoring the average tumor volume over 18 days with 2 day intervals. As shown in Fig. 5b, tumor volume increased similarly in the following three groups: (1) normal saline (control), (2) Fe_3O_4–Pd JNPs and (3) AMF + 808 nm laser irradiation. Tumors treated by PTT or MHT alone showed a little inhibitory effect, with the inhibition ratio of 25.6% and 48.6% compared with the control group, respectively. Notably, MHT + PTT treatment (with 100% tumor inhibition rate) showed the strongest anti-tumor effect,

which validated that the synergistic antitumor effect of the combination heating treatment and enhanced ROS generation triggered by AMF plus 808 nm laser irradiation. All of the tumors from various groups were collected and weighed at the end of the treatment (Fig. 5c and d). Remarkably, the MHT + PTT group displayed the best therapeutic outcome. Throughout the entire treatment, none of the mice showed significant changes in body weight (Fig. 5e). Furthermore, H&E staining results showed no obvious pathological abnormalities in the major organs, including the lungs, spleen, heart and liver of mice receiving combination treatment (MHT–PTT) (Fig. S8, ESI†), validating the safety of Fe_3O_4–Pd JNPs. To further assess the therapeutic effects of MHT + PTT therapy, the mice were monitored after treatment. We found that all the mice could survive for at least 40 days after MHT + PTT therapy, in contrast to mice in the other five treatment groups (Fig. S9, ESI†). Taken together, all of the above results documented the distinctive therapeutic efficacy of Fe_3O_4–Pd JNP mediated MHT + PTT benefiting from their synergistic heating antitumor effect and enhanced ROS generation *in vivo*.

Conclusions

In conclusion, multifunctional Fe_3O_4–Pd JNPs have been successfully constructed as novel theranostic agents that are able to realize MRI/PA guided magnetic-photo hyperthermia and chemodynamic therapy for cancer treatment. The Fe_3O_4–Pd JNPs synthesized in this work can activate H_2O_2 decomposition under an acidic environment by producing a great many tumoricidal $^{\bullet}OH$, which could be further enhanced by applying external AMF plus laser irradiation. Amplified dual-mode hyperthermia could also be achieved by Fe_3O_4–Pd JNPs at the same time. *In vivo* evaluations on 4T1 breast orthotopic tumor bearing mice demonstrated the high synergistic magnetic-photo heating and chemodynamic therapeutic efficacy of Fe_3O_4–Pd JNPs in combating cancer. Meanwhile, the intrinsic MRI/PA dual imaging capability of Fe_3O_4–Pd JNPs was used to monitor tumor accumulation of nanoparticles and thus improved the diagnostic accuracy. This work provides an alternative and highly efficient strategy for cancer therapy by rationally building the linkage between chemodynamic therapy and physical heating therapy, which is highly dependent on the unique physiochemical property of nanomaterials. Collectively, these Fe_3O_4–Pd JNPs are the first paradigm for the application of amplified magnetic-photo hyperthermia and enhanced ROS generation when applying external energy for tumor regression, providing a new avenue for efficient cancer therapy.

Conflicts of interest

There are no conflicts to declare.

Acknowledgements

References

1 O. A. Martin, R. L. Anderson, K. Narayan and M. P. Macmanus, *Nat. Rev. Clin. Oncol.*, 2017, **14**, 32–44.

2 Y.-S. Yang, R. P. Carney, S. Francesco and D. J. Irvine, *ACS Nano*, 2014, **8**, 8992–9002.

3 K. Lu, C. He, N. Guo, C. Chan, K. Ni, G. Lan, H. Tang, C. Pelizzari, Y. X. Fu and M. T. Spiotto, *et al.*, *Nat. Biomed. Eng.*, 2018, **2**, 600–610.

4 L. Liao, J. Liu, E. C. Dreaden, S. W. Morton, K. E. Shopsowitz, P. T. Hammond and J. A. Johnson, *J. Am. Chem. Soc.*, 2014, **136**, 5896–5899.

5 Y. Wen, W. Zhang, N. Gong, Y. F. Wang, H. B. Guo, W. Guo, P. C. Wang and X.-J. Liang, *Nanoscale*, 2017, **9**, 14347–14356.

6 N. Shah, A. S. Mohammad, P. Saralkar, S. A. Sprowls, S. D. Vickers, D. John, R. M. Tallman, L.-W. Brandon, K. E. Jarrell and M. Pinti, *Pharmacol. Res.*, 2018, **132**, 47–68.

7 X. Duan, C. Chan, N. Guo, W. Han, R. R. Weichselbaum and W. Lin, *J. Am. Chem. Soc.*, 2011, **138**, 16686–16695.

8 J. Beik, Z. Abed, F. S. Ghoreishi, S. Hosseini-Nami, S. Mehrzadi, A. Shakeri-Zadeh and S. K. Kamrava, *J. Controlled Release*, 2016, **235**, 205–221.

9 P. Wust, B. Hildebrandt, G. Sreenivasa, B. Rau, J. Gellermann, H. Riess, R. Felix and P. M. Schlag, *Lancet Oncol.*, 2002, **3**, 487–497.

10 W. Xue, X.-L. Liu, H. Ma, W. Xie, S. Huang, H. Wen, G. Jing, L. Zhao, X.-J. Liang and H. M. Fan, *J. Mater. Chem. B*, 2018, **6**, 2289–2303.

11 S. H. Kim, J. H. Kim and E. W. Hahn, *Radiology*, 1975, **114**, 727.

12 S. H. Noh, S. H. Moon, T. H. Shin, Y. Lim and J. Cheon, *Nano Today*, 2017, **13**, 61–76.

13 M. Johannsen, U. Gneveckow, L. Eckelt, A. Feussner, N. Waldner, R. Scholz, S. Deger, P. Wust, S. A. Loening and A. Jordan, *Int. J. Hyperthermia*, 2005, **21**, 637–647.

14 X. L. Liu, Y. Yang, C. T. Ng, L. Y. Zhao, Y. Zhang, B. H. Bay, H. M. Fan and J. Ding, *Adv. Mater.*, 2015, **27**, 1939–1944.

15 X. L. Liu and H. M. Fan, *Curr. Opin. Chem. Eng.*, 2014, **4**, 38–46.

16 J. Li, Y. Hu, J. Yang, P. Wei, W. Sun, M. Shen, G. Zhang and X. Shi, *Biomaterials*, 2015, **38**, 10–21.

17 M. Sun, L. Xu, W. Ma, X. Wu, H. Kuang, L. Wang and C. Xu, *Adv. Mater.*, 2016, **28**, 897.

18 X. Shi, H. Gong, T. Li, C. Wang, L. Cheng and Z. Liu, *Biomaterials*, 2013, **34**, 4786–4793.

19 S. P. Sherlock, S. M. Tabakman, L. Xie and H. Dai, *ACS Nano*, 2011, **5**, 1505–1512.

20 H. Yan, W. Shang, X. Sun, L. Zhao, J. Wang, Z. Xiong, Y. Jie, R. Zhang, Q. Huang and K. Wang, *et al.*, *Adv. Funct. Mater.*, 2018, **28**, 1705710.

21 D. Ling, W. Park, S.-J. Park, Y. Lu, K. S. Kim, M. J. Hackett, B. H. Kim, H. Yim, Y. S. Jeon and K. Na, *et al.*, *J. Am. Chem. Soc.*, 2014, **136**, 5647–5655.

22 L. Gao, J. Zhang, L. Nie, J. Zhang, Y. Zhang, N. Gu, T. Wang, J. Feng, D. Yang and S. Perrett, *et al.*, *Nat. Nanotechnol.*, 2007, **2**, 577–583.

23 J. Song, B. Wu, Z. Zhou, G. Zhu, Y. Liu, Z. Yang, L. Lin, G. Yu, F. Zhang and G. Zhang, *Angew. Chem.*, 2017, **56**, 8110.

24 Y. Hu, S. Mignani, J. P. Majoral, M. Shen and X. Shi, *Chem. Soc. Rev.*, 2018, **47**, 1874–1900.

25 H. Huang and J. F. Lovell, *Adv. Funct. Mater.*, 2017, **27**, 1603524.

26 R. A. Revia and M. Zhang, *Mater. Today*, 2016, **19**, 157–168.

27 X. Huang, S. Tang, X. Mu, Y. Dai, G. Chen, Z. Zhou, F. Ruan, Z. Yang and N. Zheng, *Nat. Nanotechnol.*, 2011, **6**, 28–32.

28 T. Wen, W. He, Y. Chong, Y. Liu, J. J. Yin and X. Wu, *Phys. Chem. Chem. Phys.*, 2015, **17**, 24937–24943.

29 M. Chen, S. Chen, C. He, S. Mo, X. Wang, G. Liu and N. Zheng, *Nano Res.*, 2017, **10**, 1234–1248.

30 W. W. Yu, J. C. Falkner, C. T. Yavuz and V. L. Colvin, *Chem. Commun.*, 2004, 2306–2307.

31 X. Liu, E. S. G. Choo, A. S. Ahmed, L. Y. Zhao, Y. Yang, R. V. Ramanujan, J. M. Xue, D. D. Fan, H. M. Fan and J. Ding, *J. Mater. Chem. B*, 2013, **2**, 120–128.

32 F. Liu, Y. Hou and S. Gao, *Chem. Soc. Rev.*, 2014, **43**, 8098–8113.

33 D. Ho, X. Sun and S. Sun, *Acc. Chem. Res.*, 2011, **44**, 875–882.